

# We are IntechOpen, the world's leading publisher of Open Access books Built by scientists, for scientists

6,900

Open access books available

186,000

International authors and editors

200M

Downloads

Our authors are among the

154

Countries delivered to

TOP 1%

most cited scientists

12.2%

Contributors from top 500 universities



WEB OF SCIENCE™

Selection of our books indexed in the Book Citation Index  
in Web of Science™ Core Collection (BKCI)

Interested in publishing with us?  
Contact [book.department@intechopen.com](mailto:book.department@intechopen.com)

Numbers displayed above are based on latest data collected.  
For more information visit [www.intechopen.com](http://www.intechopen.com)



---

# First-Principles Quantum Simulations of Nanoindentation

---

Qing Peng

Additional information is available at the end of the chapter

<http://dx.doi.org/10.5772/48190>

---

## 1. Introduction

Modern nanotechnology can build advanced functional materials in molecular level in nanoscales. The computer modeling and simulations are very important in such materials design. The ability to perform quantum simulations of materials properties over length scales that are relevant to experiments represents a grand challenge in computational materials science. If one could treat multi-millions or billions of electrons *effectively* at micron scales, such first-principle quantum simulations could revolutionize materials research and pave the way to the computational design of advanced materials.

There are two principal reasons why quantum simulations at relevant experimental scales are important. First of all, it allows a direct comparison between theory and experiment. For example, the rapidly emerging field of nanotechnology demands realistic and accurate modeling of material systems at the nanoscale, including nano-particles, nano-wires, quantum dots, NEMS (Nano-Electro-Mechanical Systems) and MEMS (Micro-Electro-Mechanical Systems). All these nano-systems could reach a length scale of microns and contain millions or billions of electrons, if not more. Secondly, quantum simulations at larger scales are essential even for extended bulk crystals where periodic boundary conditions may be used. This is due to the fact that a real bulk solid always contains lattice defects (or impurities) whose interactions are long range - dislocations being the prominent example. An insufficiently large periodic unit cell would lead to unrealistically high concentrations of defects and/or impurities, rendering the results of such simulations questionable.

The full knowledge of the mechanical properties of the nano-materials are very important for the advanced materials design and applications. Nanoindentation has now become a standard experimental technique for evaluating the mechanical properties of thin film materials and bulk materials in small volumes [25]. As it can measure nanometer penetration length scales, nanoindentation is an indispensable tool to assess elastic moduli and hardness of materials. It also can be used to derive strain-hardening exponents, fracture toughness, and viscoelastic properties of materials [6].

In this chapter, we will present our recent studies of nano-indentation with first-principles quantum simulations. We developed a multi-scale approach that is based *entirely* on density

functional theory (DFT) [18, 19] and allows quantum simulations at micron scale and beyond. The method, termed Quasi-continuum Density Functional Theory (QCDFT) [28–31], combines the coarse graining idea of the quasi-continuum (QC) approach and the coupling strategy of the quantum mechanics/molecular mechanics (QM/MM) method, and allows quantum simulations at the micron scale and beyond.

It should be stated at the outset that QCDFT is *not* a brute-force electronic structure method, but rather a multiscale approach that can treat large systems - effectively up to billions of electrons. Therefore, some of the electronic degrees of freedom are reduced to continuum degrees of freedom in QCDFT. On the other hand, although QCDFT utilizes the idea of QM/MM coupling, it does not involve any classical/empirical potentials (or force fields) in the formulation - the energy calculation of QCDFT is entirely based on orbital-free DFT (OFDFT). This is an important feature and advantage of QCDFT, which qualifies it as a bona fide quantum simulation method.

The QCDFT method have been used to study the nanoindentation of pure Al [30], random distributed Mg impurities in Al thin film [31], and solid solution effects on dislocation nucleation during nanoindentation [29]. The method was also applied to study the fracture in Al recently [28]. Although these works had been published before individually, a small review of this method and its applications is necessary. Here I will give an introduction to QCDFT method in Section II, especially how QCDFT evaluate the energies and forces from *ab initio* first-principles calculations. The application of QCDFT in quantum mechanical simulations of nanoindentations will be illustrated in Section III, IV and V for pure Al [30], random distributed Mg impurities in Al thin film [31], and solid solution effects on dislocation nucleation during nanoindentation [29] respectively. And finally our conclusions and outlooks of quantum mechanical simulations of nanoindentations in Sec. VI.

## 2. QCDFT methodology

In QCDFT, the degrees of freedom of the system is reduced by replacing the full set of  $N$  atoms with a small subset of  $N_r$  “representative atoms” or *repatoms* ( $N_r \ll N$ ) that approximate the total energy through appropriate weighting. This approach of reducing degrees of freedom is critical in the multiscale method and it is adopted directed from the Quasi-continuum method [32, 37, 40]. The energies of individual repatoms are computed in two different ways depending on the deformation in their immediate vicinity. Atoms experiencing large variations in the deformation gradient on an atomic scale are computed in the same way as in a standard atomistic method. In QC these atoms are called *nonlocal* atoms. In contrast, the energy of atoms experiencing a smooth deformation field on the atomic scale is computed based on the deformation gradient  $\mathbf{G}$  in their vicinity as befitting a continuum model. These atoms are called *local* atoms because their energy is based only on the deformation gradient at the point where it is computed. In a classical system where the energy is calculated based on classical/empirical inter-atomic potentials, the total energy  $E_{\text{tot}}$  can be written

$$E_{\text{tot}}^{\text{QCDFT}} = \sum_{i=1}^{N^{\text{nl}}} E_i(\mathbf{R}) + \sum_{j=1}^{N^{\text{loc}}} n_j E_j^{\text{loc}}(\mathbf{G}). \quad (1)$$

The total energy has been divided into two parts: an atomistic region of  $N^{\text{nl}}$  nonlocal atoms and a continuum region of  $N^{\text{loc}}$  local atoms ( $N^{\text{nl}} + N^{\text{loc}} = N_r$ ). The calculation in the nonlocal region is identical to that in atomistic methods with the energy of the atom depending on

the coordinates  $\mathbf{R}$  of the surrounding repatoms. Rather than depending on the positions of neighboring atoms, the energy of a local repatom depends on the deformation gradients  $\mathbf{G}$  characterizing the finite strain around its position. Then the energies and forces on the local atoms and nonlocal atoms are treated differently, but entirely on *ab initio* first-principle calculations.

In the following, we outline the energy and force formulations for both local and nonlocal regions of QCDFT. In the local region, a finite element mesh is constructed with each repatom is on the vertex of several surrounding finite elements. The energy and force of each local repatom can be obtained from the strain energy density and the stress tensor of the finite elements that share the same repatom. More specifically, according to the Cauchy-Born rule, the deformation gradient  $\mathbf{G}$  is uniform within a finite element, therefore the local energy density  $\varepsilon$  and the stress tensor for each finite element can be calculated as a perfect infinite crystal undergoing a uniform deformation specified by  $\mathbf{G}$ . In other words, one could perform an OFDFT-based energy/stress calculation for an infinite crystal by using periodic boundary conditions with the primitive lattice vectors of the deformed crystal,  $\mathbf{h}_i$  given by

$$\mathbf{h}_i = \mathbf{G} \mathbf{H}_i, \quad i = 1, 2, 3. \quad (2)$$

Here  $\mathbf{H}_i$  are the primitive lattice vectors of the undeformed crystal and the volume of the primitive unit cell is  $\Omega_0$ . The details of the OFDFT calculation can be found in Sec. II C. Once the strain energy density  $\varepsilon(\mathbf{G}_k)$  is determined, the energy contribution of the  $j$ th local repatom is given as

$$E_j^{\text{loc}}(\{\mathbf{G}\}) = \sum_{k=1}^{M_j} w_k \varepsilon(\mathbf{G}_k) \Omega_0, \quad (3)$$

where  $M_j$  is the total number of finite elements represented by the  $j$ th repatom, and  $w_k$  is the weight assigned to the  $k$ th finite element. The force on the  $j$ th local repatom is defined as the gradient of the total energy with respect to its coordinate  $\mathbf{R}_j^{\text{loc}}$ . In practice, the nodal force on each finite element is calculated from the stress tensor of the finite element by using the principle of virtual work [47]. The force on the repatom is then obtained by summing the nodal force contributions from each surrounding finite elements.

For the energy/force calculation in the nonlocal region, we resort to a novel QM/MM approach that was developed recently for metals [43, 44]. The coupling between the QM and MM regions is achieved quantum mechanically within an OFDFT formulation. Although the detailed implementation of the QM/MM approach is presented in Sec. II D, we wish to stress two important points here: (1) The original QC formulation assumes that the total energy can be written as a sum over individual atomic energies. This condition is not satisfied by quantum mechanical models. The energy of the nonlocal region is now a functional of total electron density, so instead of the expression in Eq. 1, the total energy of QCDFT should be expressed as:

$$E_{\text{tot}}^{\text{QCDFT}} = E^{\text{nl}}[\rho^{\text{tot}}] + \sum_{j=1}^{N^{\text{loc}}} n_j E_j^{\text{loc}}(\{\mathbf{G}\}). \quad (4)$$

Here  $\rho^{\text{tot}}$  is the total electron density in the nonlocal region as well as the coupling nonlocal/local region i.e., the buffer region in the following discussion. (2) The nonlocal energy,  $E^{\text{nl}}$  should be calculated with appropriate boundary conditions; that is to say, it should

include the interaction energy between the nonlocal atoms and neighboring local atoms. In the original QC framework, this requirement is realized by including dummy atoms in the energy/force calculation of a given nonlocal repatom. These dummy atoms are in the local region and within the cut-off radius of the given nonlocal repatom. The dummy atoms are not independent degrees of freedom in the local region, but rather slaves to the local repatoms. In this way, the nonlocal calculation is carried out with the appropriate boundary conditions, and at the same time, the energy of the dummy atoms is still treated with the Cauchy-Born rule, consistent with their status. In the QCDFD approach, a buffer region including the dummy atoms and local repatoms that are adjacent to the nonlocal repatoms is selected as the “MM” region, and the nonlocal atoms constitute the QM region. The nonlocal atoms are treated by OFDFT, and the coupling between the “MM” and QM region is also formulated within OFDFT. Therefore the entire system is formulated with one energy functional, OFDFT. Note that “MM” here is actually a misnomer: the local atoms are treated by OFDFT with the Cauchy-Born rule as mentioned earlier, and we retain the designation “MM” solely to indicate the similarity to the earlier coupling scheme [43, 44].

The nonlocal region is modeled at the atomistic level with a QM/MM approach. In a typical QM/MM calculation, the system is partitioned into two separated domains: a QM region and an MM region. In QCDFD, the QM region refers to the nonlocal region and the MM region refers to the buffer region. The buffer region is introduced to provide the boundary conditions for the calculation of nonlocal energy and it contains both dummy atoms and local repatoms. The dummy atoms differ from the local and nonlocal repatoms in the following sense: (1) their positions are interpolated from the positions of local repatoms using finite element shape functions; (2) the energy and force on the dummy atoms does not need to be considered explicitly since they are not explicit degrees of the freedom in the QC formulation.

At present, there are two types of QM/MM coupling strategies: mechanical coupling and quantum coupling [7, 22, 24, 34, 36, 45]. The interaction energy between the QM and MM regions is formulated at the MM level for mechanical coupling, and at the QM level for quantum coupling. Although mechanical coupling is much simpler than quantum coupling, it has many drawbacks - the most important one being that the electronic interaction between the two regions is ignored. For example, with mechanical coupling, electrostatic, kinetic, and exchange-correlation interaction energies are not considered explicitly. As a consequence, the physics of the QM region is not accurately captured. Another problem with mechanical coupling is that the reliability and availability of empirical potentials for treating the coupling are severely limited. In contrast, quantum coupling should be more accurate as it accounts for all quantum mechanical interaction terms. Depending on the level of the quantum description, the extent of the electronic coupling varies from merely long-range electrostatic interaction to a full Coulomb interaction, including short-ranged exchange-correlations [7, 22].

In the present QCDFD method, we use an OFDFT-based quantum mechanical QM/MM coupling proposed by Zhang and Lu [43, 44] which considers the full Coulomb, kinetic energy, and exchange-correlation interactions. More specifically, both the energy of the nonlocal atoms and the interaction energy between the nonlocal atoms and the buffer atoms are calculated by OFDFT. To simplify the notation, we denote the nonlocal region as region I, and the buffer region as region II. Typically, the buffer region consists of several atomic layers surrounding the nonlocal region. The nonlocal energy  $E^{\text{nl}}$  as defined in Eq. (4) can be expressed as:

$$E^{\text{nl}}[\rho^{\text{tot}}] = \min_{\rho^{\text{I}}} \{E_{\text{OF}}[\rho^{\text{I}}; \mathbf{R}^{\text{I}}] + E_{\text{OF}}^{\text{int}}[\rho^{\text{I}}, \rho^{\text{II}}; \mathbf{R}^{\text{I}}, \mathbf{R}^{\text{II}}]\}. \quad (5)$$

where  $\mathbf{R}^{\text{I}}$  and  $\mathbf{R}^{\text{II}}$  denote ionic coordinates in region I and II respectively. The OFDFT energy functional  $E_{\text{OF}}$  is obtained routinely [13–15, 21, 23, 30, 41]. The total charge density of the QM/MM system  $\rho^{\text{tot}}$  consists of two contributions:  $\rho^{\text{tot}} = \rho^{\text{I}} + \rho^{\text{II}}$  where  $\rho^{\text{I}}$  and  $\rho^{\text{II}}$  represent the charge density from region I and II respectively. While  $\rho^{\text{I}}$  is determined self-consistently by minimizing the total energy functional Eq. (5),  $\rho^{\text{II}}$  is defined as a superposition of atom-centered charge densities  $\rho^{\text{at}}$  via  $\rho^{\text{II}}(\mathbf{r}) = \sum_{i \in \text{II}} \rho^{\text{at}}(\mathbf{r} - \mathbf{R}_i)$ . Note that  $\rho^{\text{at}}$  is spherically symmetric and can be constructed *a priori*. It is important to point out that  $\rho^{\text{at}}$  is *not* a charge density of an isolated atom, but rather an atom-centered charge density whose superposition gives rise to the correct bulk density of region II [43]. Therefore  $\rho^{\text{II}}(\mathbf{r})$  is fixed for a given ionic configuration of region II and it changes upon the motion of region II ions. In other words, the electronic degree of freedom in the formulation is  $\rho^{\text{I}}$  only and  $\rho^{\text{II}}$  is fixed during the electronic relaxation. The interaction energy is thus defined as following:

$$\begin{aligned} E_{\text{OF}}^{\text{int}}[\rho^{\text{I}}, \rho^{\text{II}}; \mathbf{R}^{\text{I}}, \mathbf{R}^{\text{II}}] &= E_{\text{OF}}[\rho^{\text{tot}}; \mathbf{R}^{\text{tot}}] - E_{\text{OF}}[\rho^{\text{I}}; \mathbf{R}^{\text{I}}] \\ &\quad - E_{\text{OF}}[\rho^{\text{II}}; \mathbf{R}^{\text{II}}], \end{aligned} \quad (6)$$

where  $\mathbf{R}^{\text{tot}} \equiv \mathbf{R}^{\text{I}} \cup \mathbf{R}^{\text{II}}$ . The energy functional of Eq. (5) can be written as

$$E^{\text{nl}}[\rho^{\text{tot}}] = \min_{\rho^{\text{I}}} \{E_{\text{OF}}[\rho^{\text{tot}}; \mathbf{R}^{\text{tot}}] - E_{\text{OF}}[\rho^{\text{II}}; \mathbf{R}^{\text{II}}]\}. \quad (7)$$

A basic ansatz of the present QM/MM formulation (Eq. (7)) is that  $\rho^{\text{I}}$  must be confined within a finite volume ( $\Omega^{\text{I}}$ ) that is necessarily *larger* than region I but much smaller than the entire QM/MM region. In addition, since some terms in the formulation Eq. (7) could be more efficiently computed in reciprocal space (discussed in the following), we also introduce a volume  $\Omega^{\text{B}}$  over which the periodic boundary conditions are applied. The periodic box  $\Omega^{\text{B}}$  should be larger than  $\Omega^{\text{I}}$  so that  $\rho^{\text{I}}$  does not overlap with its periodic images [43]. Note that the QM/MM system is only a small fraction of the entire QCDFD system. To facilitate the introduction of the QCDFD method, we present a schematic diagram in Fig. (1) which demonstrates the typical partition of domains in a QCDFD calculation. This particular example is for a nanoindentation calculation of an Al thin film which is used to validate the QCDFD method (see Sec. III for details). The lower-right panel shows the entire system and the corresponding finite element mesh. The lower-left panel is a blow-up view of the entire system, which is further zoomed in as shown in the upper-left panel, focusing on the nonlocal region. The upper-right panel shows out-of-plane displacements of the nonlocal atoms, where the dislocations and the stacking faults are clearly visible. All lengths are given in Å. The blue and green circles represent the nonlocal and buffer atoms, respectively. The volumes  $\Omega^{\text{I}}$  and  $\Omega^{\text{B}}$  are represented by the black dash box and solid box in the upper-left panel, respectively. There is no constraint on  $\rho^{\text{II}}$ , which can extend to the entire QM/MM system. In addition to its computational efficiency as discussed in Sec. II B, OFDFT allows Eq. (7) to be evaluated over  $\Omega^{\text{I}}$  rather than over the entire QM/MM system as Eq. (7) appears to suggest [3, 43]. This significant computational saving is due to the cancellation in evaluating the first and second term of Eq. (7), and it is rendered by the orbital-free nature of OFDFT and the localization of  $\rho^{\text{I}}$ .

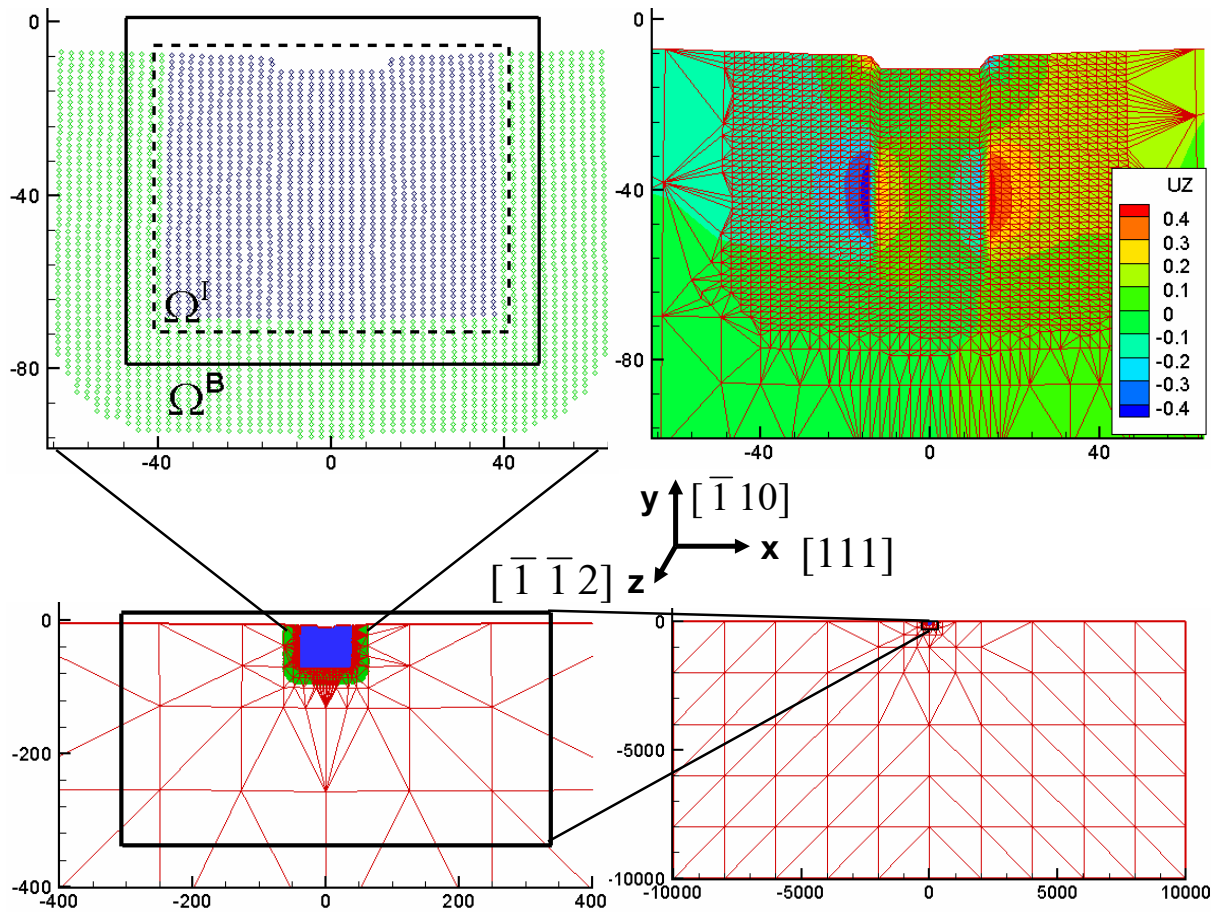


**Figure 1.** (Color online) The overview of the entire system and domain partition in QCDFT with nanoindentation as an example. The  $x$ ,  $y$  and  $z$  axes are along  $[111]$ ,  $[\bar{1}10]$ , and  $[\bar{1}\bar{1}2]$ , respectively.  $\Omega^I$  and  $\Omega^B$  are  $2.8 \text{ \AA}$  and  $8 \text{ \AA}$  beyond the nonlocal region in  $\pm x$  and  $\pm y$  directions, respectively [43]. The colors indicate  $u_z$ , the out-of-plane displacement of atoms in the  $z$ -direction.

## 2.1. Ghost forces

In the QC method, the entire system is divided into two regions - local and nonlocal - and thus an artificial interface is introduced. The atoms in these two regions are modeled differently: in the local continuum region, the energy depends only on the deformation gradient, while in the nonlocal atomistic region, the energy depends on the position of the atoms. There is an inherent mismatch of the energy functional between the local and nonlocal regions. As a result, a well-defined energy functional for the entire QC model will lead to spurious forces near the interface, called “ghost forces” in the QC literature. Note that the ghost force only exists on local repatoms adjacent to the local/nonlocal (or QM/MM) interface. The principal reason for the ghost force is that we choose to focus on approximating the energy and not the force. One could opt to avoid the ghost force by formulating the force appropriately, but then one could no longer define an appropriate total energy of the system. There are two advantages of having a well-defined energy in atomistic simulations: (1) it is numerically more efficient to minimize energy, compared to the absolute value of a force; (2) one can potentially obey an energy conservation law in dynamical simulations.

In the QCDFT (or the QM/MM) approach, the ghost force is defined as the force difference between two distinctive formulations: (1) where the force is calculated by applying the

Cauchy-Born rule throughout the entire system; this corresponds to a “consistent” way of calculating force, thus no ghost force exists and (2) where the force is calculated based on the mixed local/nonlocal formulation aforementioned and hence the ghost force exists. In the first case, the force on a local repatom would be

$$\tilde{\mathbf{F}}(\mathbf{R}^{\text{II}}) = -\frac{\partial E_{\text{CB}}(\mathbf{R}^{\text{tot}})}{\partial \mathbf{R}^{\text{II}}}, \quad (8)$$

where  $E_{\text{CB}}(\mathbf{R}^{\text{tot}})$  is the total energy of the system where the Cauchy-Born rule is used throughout. In the second case, the total energy of the QM/MM system can be written as:

$$E^{\text{tot}}(\mathbf{R}^{\text{tot}}) = E_{\text{CB}}(\mathbf{R}^{\text{II}}) + E_{\text{QM}}(\mathbf{R}^{\text{I}}) + E_{\text{QM}}^{\text{int}}(\mathbf{R}^{\text{tot}}), \quad (9)$$

where  $E_{\text{CB}}(\mathbf{R}^{\text{II}})$  is the local energy computed using the Cauchy-Born rule,  $E_{\text{QM}}(\mathbf{R}^{\text{I}})$  is the nonlocal energy computed by a quantum mechanical approach, and  $E_{\text{QM}}^{\text{int}}(\mathbf{R}^{\text{tot}})$  is the quantum mechanical interaction energy. The force derived from this total energy functional is

$$\begin{aligned} \mathbf{F}(\mathbf{R}^{\text{II}}) &= -\frac{\partial E_{\text{CB}}(\mathbf{R}^{\text{II}})}{\partial \mathbf{R}^{\text{II}}} - \frac{\partial E_{\text{QM}}^{\text{int}}(\mathbf{R}^{\text{tot}})}{\partial \mathbf{R}^{\text{II}}} \\ &= -\frac{\partial E_{\text{CB}}(\mathbf{R}^{\text{tot}})}{\partial \mathbf{R}^{\text{II}}} + \frac{\partial E_{\text{CB}}^{\text{int}}(\mathbf{R}^{\text{tot}})}{\partial \mathbf{R}^{\text{II}}} - \frac{\partial E_{\text{QM}}^{\text{int}}(\mathbf{R}^{\text{tot}})}{\partial \mathbf{R}^{\text{II}}} \\ &= \tilde{\mathbf{F}}(\mathbf{R}^{\text{II}}) + \mathbf{F}^{\text{ghost}}, \end{aligned} \quad (10)$$

where  $E_{\text{CB}}^{\text{int}}(\mathbf{R}^{\text{tot}}) = E_{\text{CB}}(\mathbf{R}^{\text{tot}}) - E_{\text{CB}}(\mathbf{R}^{\text{I}}) - E_{\text{CB}}(\mathbf{R}^{\text{II}})$  is the interaction energy calculated with the Cauchy-Born rule applied to the entire system, and  $\mathbf{F}^{\text{ghost}} = \frac{\partial \{E_{\text{CB}}^{\text{int}}(\mathbf{R}^{\text{tot}}) - E_{\text{QM}}^{\text{int}}(\mathbf{R}^{\text{tot}})\}}{\partial \mathbf{R}^{\text{II}}}$  is the ghost force. Note that  $E_{\text{CB}}(\mathbf{R}^{\text{I}})$  does not depend on  $\mathbf{R}^{\text{II}}$ , hence its contribution to force is zero.

Having determined the ghost force in QCDFE, one can correct for it by adding a correction force  $\mathbf{F}^{\text{corr}} = -\mathbf{F}^{\text{ghost}}$  on the local atoms ( $\mathbf{F}^{\text{corr}} + \mathbf{F}(\mathbf{R}^{\text{II}})$ ) so that the resultant force is  $\tilde{\mathbf{F}}(\mathbf{R}^{\text{II}})$ . The correction force is applied to the local repatoms as a dead load, computed each time the status of the representative atoms is updated, and remains fixed until the next update required due to the evolving state of deformation. In practice, the correction force is nonzero only for the local repatoms adjacent to the nonlocal region. Finally, the total energy expression has to be modified accordingly so that its gradient is consistent with the new formulation of force. This is achieved by incorporating the work done by the correction force into the original energy formulation:

$$\tilde{E}^{\text{tot}} = E^{\text{tot}} - \sum_{\alpha}^{N'_{\text{rep}}} \mathbf{F}_{\alpha}^{\text{corr}} \cdot \mathbf{u}_{\alpha}, \quad (11)$$

where  $N'_{\text{rep}}$  denotes the number of local repatoms whose correction force is nonzero, and  $\mathbf{u}_{\alpha}$  is the displacement of the  $\alpha$ th local repatom.

## 2.2. Parallelization of QCDFE

The present QCDFE code is parallelized based on the Message Passing Interface (MPI). The parallelization is achieved for both local and nonlocal calculations. The parallelization for the local part is trivial: since the energy/force calculation for each finite element is independent from others, one can divide the local calculations evenly onto each processor. The computational time is thus proportional to the ratio of the number of the local finite elements to the available processors. Parallelization of the nonlocal region is achieved through domain decomposition, since the calculations (e.g. charge density, energy and force computations) are all performed on real space grids, except the convolution terms in the kinetic energy. Grid points are evenly distributed to available processors, and results are obtained by summing up contributions from all grids. The calculation of the convolution terms is performed by parallelized FFT.

The speedup using parallelization in local part is linear. The nonlocal part is dependent on the nodes used. In our calculations, an overall of about 26 times speedup was achieved when the program runs on 32 nodes.

## 2.3. Model setup

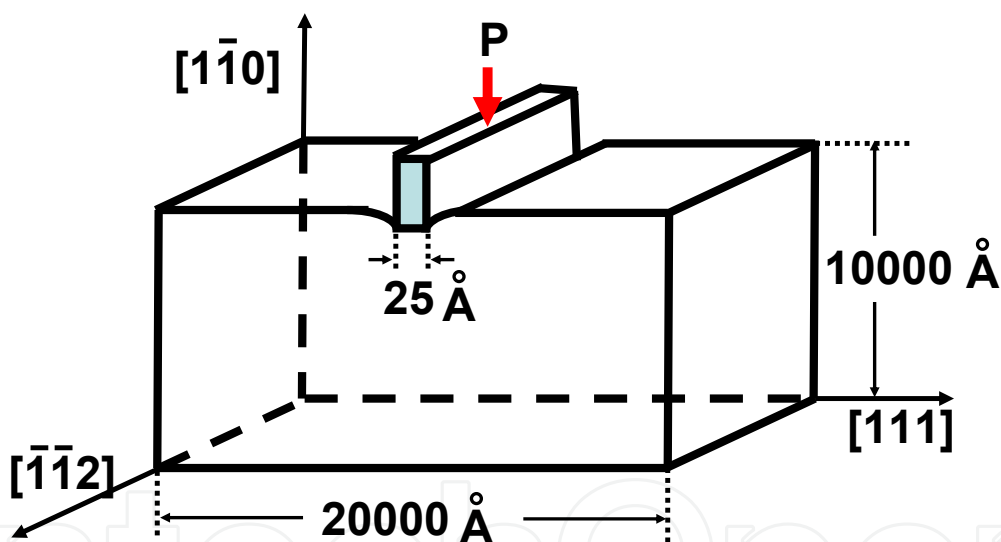


**Figure 2.** Schematic representation of the nanoindentation of Al thin film: geometry and orientation

Nanoindentation has now become a standard experimental technique for evaluating the mechanical properties of thin film materials and bulk materials in small volumes [25]. As it can measure nanometer penetration length scales, nanoindentation is an indispensable tool to assess elastic moduli and hardness of materials. It also can be used to derive strain-hardening exponents, fracture toughness, and viscoelastic properties of materials [6]. Moreover, nanoindentation also provides an opportunity to explore and better understand the elastic limit and incipient plasticity of crystalline solids [46]. For example, homogeneous nucleation of dislocations gives rise to the instability at the elastic limit of a perfect crystal. Exceeding the elastic limit can be manifested by a discontinuity in the load-displacement curve in a nanoindentation experiment [4, 8, 11, 26, 27, 35]. The onset of the discontinuity is

an indication that the atomically localized deformation, such as dislocation nucleation occurs beneath the indenter. This correlation has been well established from both experimental and computational perspectives. For example, an *in situ* experiment by Gouldstone *et al.* using the Bragg-Nye bubble raft clearly demonstrated that homogeneous nucleation of dislocations corresponds to the discontinuity of the load-depth curve [12]. MD simulations have led to greater insight into the atomistic mechanism of nanoindentation [16, 48]. In particular, several QC simulations have been carried out for nanoindentation in Al thin films [13, 14, 17, 33, 39]. Tadmor *et al.* have used Embedded atom method based QC (EAM-QC) to study nanoindentation with a knife-like indenter with a pseudo-two-dimension (2D) model [39]. They observed the correspondence between the discontinuity in the load-displacement curve with the onset of plasticity. By using a much larger spherical indenter (700 nm), Knap *et al.* discovered that plasticity could occur without the corresponding discontinuity in the load-displacement curve [17]. However, when the indenter size was reduced (to 70 nm) the discontinuity reappeared. More recently, Hayes *et al.* have performed local OFDFT- and EAM-based QC calculations for nanoindentation of Al with a spherical indenter of 740 nm in radius [13, 14]. Using elastic stability criteria, they predicted the location of dislocation nucleation beneath the indenter, and obtained different results from EAM and OFDFT local QC calculations. Since many QC simulations have been carried out for nanoindentation of Al, it is not the purpose of the present paper (and we do not expect) to discover any new physics with QCDFD calculations. Instead, we use nanoindentation as an example to demonstrate the validity and the usefulness of the QCDFD method.

The present QCDFD approach is applied to nanoindentation of an Al thin film resting on a rigid substrate with a rigid knife-like indenter. The QC method is appropriate for the problem because it allows the modeling of system dimensions on the order of microns and thus minimizes the possibility of contaminating the results by the boundary conditions arising from small model sizes typically used in MD simulations. We chose this particular system for two reasons. First, there exists a good local pseudo-potential [9] and an excellent EAM potential [5] for Al. Secondly, results from conventional EAM-based QC simulations can be compared to the present calculations. An ideal validation of the method would require a full-blown OFDFT atomistic simulation for nanoindentation, which is not yet attainable. The second best approach would be a conventional QC simulation with an excellent EAM potential that compares well to OFDFT in terms of critical materials properties relevant to nanoindentation. Our reasoning is that the conventional QC method has been well established; thus as long as the EAM potential used is reliable, then the EAM-QC results should be reliable as well. In this paper, we have rescaled the “force-matching” EAM potential of Al [5] so that it matches precisely the OFDFT value of the lattice constant and bulk modulus of Al [3].

The crystallographic orientation of the system is displayed in Fig. (2). The size of the entire system is  $2 \mu\text{m} \times 1 \mu\text{m} \times 4.9385 \text{ \AA}$  along the [111] (x direction), the  $[\bar{1}10]$  (y direction), and the  $[\bar{1}\bar{1}2]$  (z direction), respectively. The system is periodic in the z-dimension, has Dirichlet boundary conditions in the other two directions, and contains over 60 million Al atoms - a size that is well beyond the reach of any full-blown brute-force quantum calculation. The thickness of the thin film is selected to be comparable to the typical dislocation separation distance in well-annealed metals, which is of the order  $1 \mu\text{m}$ . The unloaded system is a perfect single crystal similar to the experimental situation under the nanoindenter. The film is oriented so that the preferred slip system  $\langle 110 \rangle \{111\}$  is parallel to the indentation direction to facilitate dislocation nucleation. The indenter is a rigid flat punch of width  $25 \text{ \AA}$ . We assume the

perfect-stick boundary condition for the indenter so that the Al atoms in contact with it are not allowed to slip. The knife-like geometry of the indenter is dictated by the pseudo-2D nature of the QC model adopted. Three-dimensional QC models do exist and can be implemented in QCDFD [13, 14, 17]. We chose to work with the pseudo-2D model in this example for its simplicity. The prefix *pseudo* is meant to emphasize that although the analysis is carried out in a 2D coordinate system, out-of-plane displacements are allowed and all atomistic calculations are three-dimensional. Within this setting only dislocations with line directions perpendicular to the  $xy$  plane can be nucleated. The elastic moduli of  $C_{12}$ ,  $C_{44}$ ,  $C_{11}$  of Al are computed from three deformation modes, including hydrostatic, volume-conserving tetragonal and volume-conserving rhombohedral deformations. The shear modulus  $\mu$  and Poisson's ratio  $\nu$  are computed from the elastic moduli by a Voigt average:  $\mu = (C_{11} - C_{12} + 3C_{44})/5$  and  $\nu = \frac{C_{11} + 4C_{12} - 2C_{44}}{2(C_{11} + 3C_{12} + C_{44})}$ . The values are listed in Table (1).

## 2.4. Loading procedure

The simulation is performed quasi-statically with a displacement control where the indentation depth ( $d$ ) is increased by 0.2 Å at each loading step. We also tried a smaller loading step of 0.1 Å and obtained essentially the same results. Because OFDFT calculations are still much more expensive than EAM, we use EAM-based QC to relax the system for most of the loading steps. For load  $d = 0$ , the QCDFD calculation is performed to account for surface relaxations. From the resultant configuration, the depth of the indenter  $d$  is increased to 0.2 Å, again relaxed by QCDFD. After that, the calculations are done solely by EAM-QC except for the loading steps at  $d = 1.8, 3.8, 9.2$  Å, when the corresponding EAM configurations are further relaxed by QCDFD. The onset of plasticity occurs at  $d = 9.4$  Å. We increased the indenter depth of 0.2 Å from the relaxed QCDFD configuration at  $d = 9.2$  Å, and then performed a QCDFD calculation to obtain the final structure at  $d = 9.4$  Å. Such a simulation strategy is justified based on two considerations: (1) An earlier nanoindentation study of the same Al surface found that the onset of plasticity occurred at a smaller load with EAM-based local QC calculations comparing to OFDFT calculations [13]. The result was obtained by a local elastic stability analysis with EAM and OFDFT calculations of energetics and stress. The result suggests that we will not miss the onset of plasticity with the present loading procedure by performing EAM-QC relaxations preceding QCDFD. (2) Before the onset of plasticity, the load-displacement response is essentially linear with the slope determined by the elastic properties of the material. In other words, two QCDFD data points would be sufficient to obtain the correct linear part of the curve. Moreover, the fact that the EAM potential used in this study yields rather similar elastic constants to those from OFDFT suggests that the mixed EAM/OFDFT relaxation should not introduce large errors in the results.

## 2.5. Computation parameters

In Fig. (1), we present a schematic diagram illustrating the partition of domains for a QCDFD simulation of nanoindentation. The system shown in the diagram contains 1420 nonlocal repatoms, 736 local repatoms and 1539 finite elements, and is periodic along the  $z$  direction. The top surface is allowed to relax during the calculations while the other three surfaces of the sample are held fixed.

The parameters of the density-dependent kernel are chosen from reference [42], and Al ions are represented by the Goodwin-Needs-Heine local pseudo-potential [9]. The high kinetic

energy cutoff for the plane wave basis of 1600 eV is used to ensure the convergence of the charge density. For the nonlocal calculation, the grid density for the volume  $\Omega^I$  is 5 grid-points per Å. The  $\Omega^I$  box goes beyond the nonlocal region by 8 Å in  $\pm x$  and  $\pm y$  directions so that  $\rho^I$  decays to zero at the boundary of  $\Omega^I$ . The relaxation of all repatoms is performed by a conjugate gradient method until the maximum force on any repatom is less than 0.03 eV/Å.

At beginning of the simulation, the number of nonlocal repatoms is rather small,  $\sim 80$ . As the load increases, the material deforms. When the variation of the deformation gradient between neighboring finite elements reaches 0.15, the mesh is refined, and the number of repatoms grows. The partitions, i.e. the size of nonlocal DFT region also grows. Close to the onset of plasticity, the number of nonlocal DFT atoms reaches 1420. The energy functionals are the same for all the regions in these studies.

In order to validate the QCDF method, we performed EAM-QC calculations of the nanoindentation with the same loading steps. We also calculated some relevant material properties using the rescaled EAM and OFDFT method for bulk Al. The computational results along with experimental values extrapolated to T=0 K [5] are listed in Table (1). These numbers could shed light on the nanoindentation results from the QCDF calculations.

	OFDFT	rescaled EAM	Experiment	(Unit)
elastic modulus $C_{11}$	117.17	97.13	118.0	GPa
elastic modulus $C_{12}$	41.36	51.16	62.4	GPa
elastic modulus $C_{44}$	29.76	30.23	32.5	GPa
Bulk modulus $E$	66.63	66.48	80.93	GPa
shear modulus $\mu$	33.01	27.33	30.62	GPa
Poisson's ratio $\nu$	0.287	0.319	0.332	
lattice constant $a_0$	4.032	4.032	4.032	Å
surface energy $\gamma_{111}$	0.867	0.72	1.14-1.2	J/m <sup>2</sup>
stacking fault energy	0.10	0.10	0.12-0.14	J/m <sup>2</sup>

**Table 1.** Elastic moduli, Poisson's ratio, lattice constant, (111) surface energy, and intrinsic stacking fault energy obtained by OFDFT and EAM calculations on bulk Al, and the corresponding experimental values extrapolated to T=0 K.

It is worth to note that the such quasi-2D simulations blocked the dislocations inclined in the third dimension. As a result, the twin formation may occur at a high loading rate and low temperature, compared with dislocation slip. Such quasi-2D limitations, however, could be validated in the systems where grain boundaries provides such geometrical confinement. For example, the deformation twinning has been observed in experimental studies of nanocrystalline Aluminum when the grain size is down to tens of nanometers[2, 20].

### 3. Quantum mechanical simulation of pure aluminum

The load-displacement curve is the typical observable for nanoindentation, and is widely used in both experiment and theory, often serving as a link between the two. In particular, it is conventional to identify the onset of plasticity with the first jump in the load-displacement curve during indentation [4, 10, 11, 13, 17, 33, 35, 39, 46]. In the present work, the loads are given in N/m, normalized by the length of the indenter in the out-of-plane direction.

Let us first discuss the QC results with the rescaled EAM potential. The load-displacement ( $P - d$ ) curve shows a linear relation followed by a discrete drop at  $d = 9.4 \text{ \AA}$ , shown by the dashed line in Fig. (8). The drop corresponds to the homogeneous nucleation of dislocations beneath the indenter - the onset of plasticity. A pair of straight edge dislocations is nucleated at  $x = \pm 13 \text{ \AA}$ , and  $y = -49 \text{ \AA}$ . In Fig. (9), we present the out-of-plane (or screw) displacement  $u_z$  of the nonlocal repatoms. The nonzero screw displacement of edge dislocations suggests that each dislocation is dissociated into two  $1/6 \langle 112 \rangle$  Shockley partials bound by a stacking fault with a width of about  $14 \text{ \AA}$ . An earlier EAM-QC calculation [39] which has the same geometry as the present model but with a thinner sample (the thickness was ten times smaller than the present case), yields a separation distance of  $13.5 \text{ \AA}$ . The activated slip planes are those  $\{111\}$  planes that are adjacent to the side surfaces of the indenter. The linear relation in the  $P - d$  curve is due to: (1) the elastic response of the material before the onset of plasticity and (2) the particular choice of the rectangular indenter; a spherical indenter would have given rise to a parabolic  $P - d$  curve [11, 13]. The slope for the linear part of the curve is  $20.8 \text{ GPa}$ , which is less than the shear modulus and  $C_{44}$ . The critical load,  $P_{cr}$  for homogeneous dislocation nucleation is  $18.4 \text{ N/m}$ , corresponding to a hardness of  $7.3 \text{ GPa}$ . Earlier EAM-QC calculations predicted the hardness to be  $9.8 \text{ GPa}$  [39]. The drop in applied load due to the nucleation of dislocations is  $\Delta P = 3.4 \text{ N/m}$ . The value of  $\Delta P$  from the previous EAM-QC calculation is  $10 \text{ N/m}$  [39], which is three times of the present result. Using the same sample size as in [39], we found  $\Delta P = 9.02 \text{ N/m}$ , which is very close to the value reported in [39]. Thus, the discrepancy of  $\Delta P$  is mainly due to the different sample sizes used in the two calculations indicating the importance of simulations at length scales relevant to experiments.

For QCDFT calculations, the load-displacement curve shows a linear relation up to a depth of  $9.2 \text{ \AA}$ , followed by a drop at  $d = 9.4 \text{ \AA}$ , shown by the solid line in Fig. (8). The slope of initial linear part of the load-displacement curve is  $23.9 \text{ GPa}$ , rather close to the corresponding EAM value. The maximum load in linear region is  $P_{cr} = 21.4 \text{ N/m}$ , corresponding to a hardness of  $8.6 \text{ GPa}$ . The fact that OFDFT predicts a larger  $P_{cr}$  than EAM is consistent with the results of Hayes *et al.* using local QC simulations for the same Al surface [13]. A pair of edge dislocations is nucleated at  $x = \pm 13 \text{ \AA}$ , and  $y = -50 \text{ \AA}$ . The partial separation distance is about  $19 \text{ \AA}$ , larger than the corresponding EAM value. The drop in the applied load due to dislocations nucleation is  $7.8 \text{ N/m}$ , which is more than twice of the corresponding EAM value. The large difference in  $\Delta P$  between QCDFT and EAM-QC is interesting. It may suggest that although OFDFT and EAM produce rather similar results before the onset of plasticity, they differ significantly in describing certain aspects of defect properties. In particular, although both methods predict almost the same location for dislocation nucleation, they yield sizeable differences in partial dislocation width and  $\Delta P$ . This result justifies the use of more accurate quantum simulations such as KS-DFT for nonlocal region where defects are present. Overall, we find that QCDFT gives very reasonable results comparing to the conventional EAM-QC. Although more validations are underway, we are optimistic that the QCDFT method is indeed reliable and offers a new route for quantum simulation of materials at large length scales.

#### 4. Random distributed magnesium impurities in aluminum thin film

The effect of Mg impurities on the ideal strength and incipient plasticity of the Al thin film. In the calculations, five Mg impurities are introduced randomly below the indenter, as schematically shown in Fig. (5). The results of the randomly distributed Mg impurities are referred as *random*, distinguishing from the results of the pure system, referred as *pure*. At

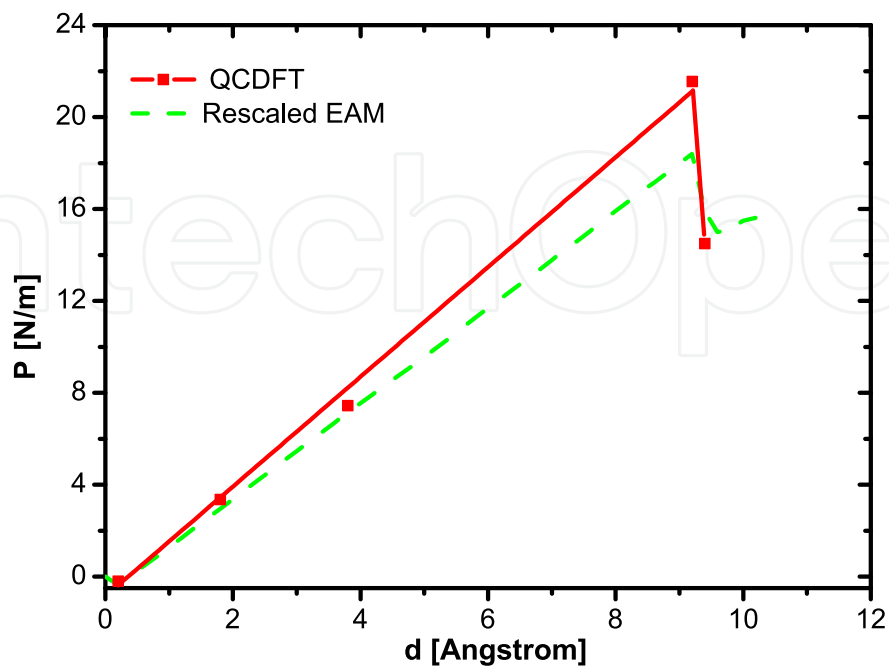


**Figure 3.** Load-displacement curve for nanoindentation of an Al thin film with a rigid rectangular indenter: with QCDFT (red solid line) and rescaled EAM-QC (green dashed line). The red squares are actual QCDFT data points and the solid line is the best fit to the data points. All EAM-QC data points are on the dashed line.

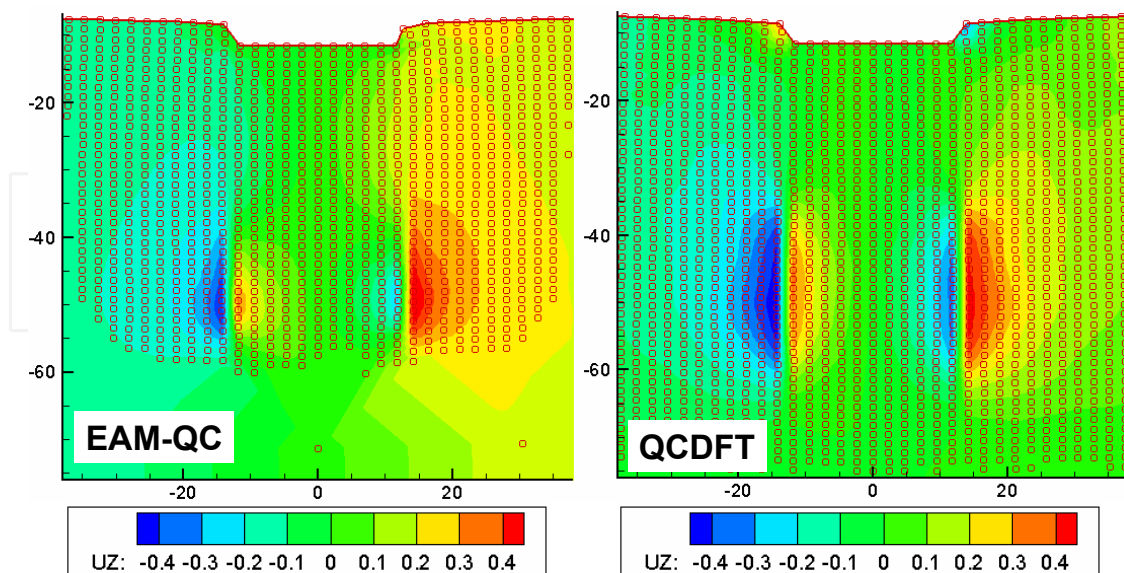


**Figure 4.** The out-of-plane displacement  $u_z$  obtained from the rescaled EAM-QC (left) and QCDFT (right) calculations. The circles represent the repatoms and the displacement ranges from -0.4 (blue) to 0.4 (red) Å.

$d = 3.0, 6.0, 7.5 \text{ \AA}$ , the *random* results are obtained after full relaxations of the *pure* Al system. The QCDFT loading is carried out after  $d = 7.5 \text{ \AA}$  starting from the full relaxed configuration of a previous loading step, until the onset of the plasticity occurs at  $d = 8.1 \text{ \AA}$ .

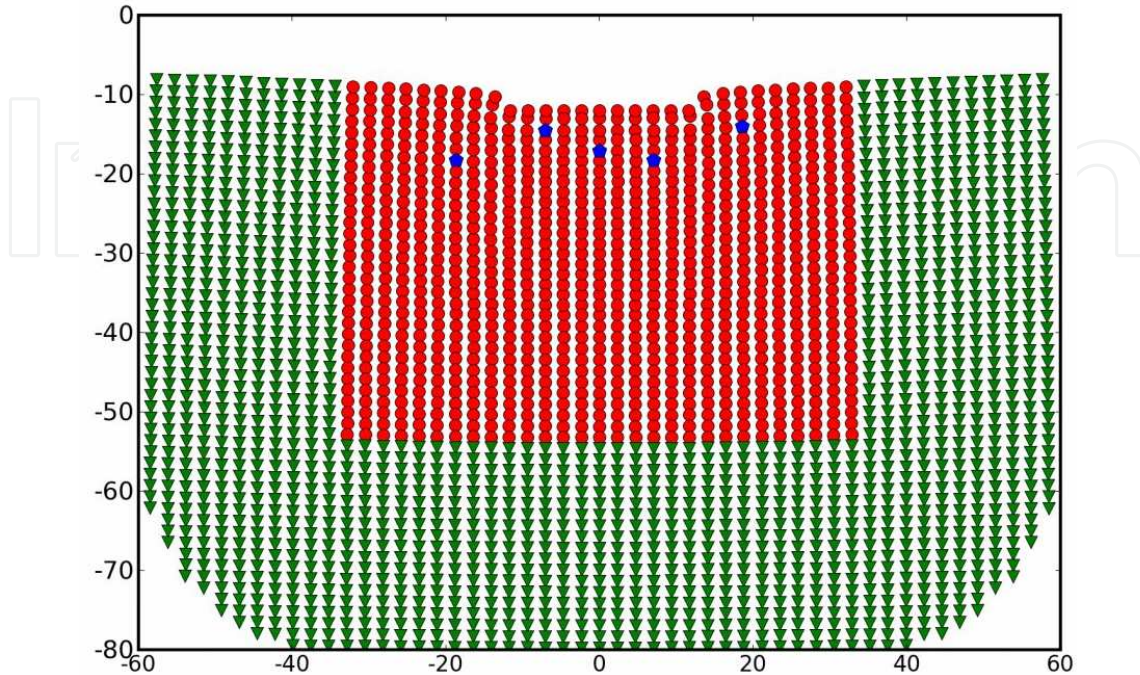


**Figure 5.** Schematic diagram of the randomly distributed Mg impurities in the Al thin film. The red spheres and blue pentagons represent nonlocal Al and Mg atoms, respectively. The green triangle represents Al buffer atoms. The dimensions are given in  $\text{\AA}$ .

The load-displacement curve is the typical observable for nanoindentation, and is widely used in both experiment and theory, often serving as a link between the two. In particular, it is conventional to identify the onset of incipient plasticity with the first drop in the load-displacement curve during indentation [4, 10, 11, 13, 17, 30, 33, 35, 39, 46]. In the present work, the load is given in N/m, normalized by the length of the indenter in the out-of-plane direction.

For pure Al, the load-displacement ( $P - d$ ) curve shows a linear relation followed by a drop at  $d = 8.2 \text{ \AA}$ , shown by the dashed line in Fig. (8). The drop corresponds to the homogeneous nucleation of dislocations beneath the indenter - the onset of plasticity. A pair of straight edge dislocations are nucleated at  $x = \pm 13 \text{ \AA}$ , and  $y = -50 \text{ \AA}$ . In Fig. (9), we present the out-of-plane (or screw) displacement  $u_z$  of the nonlocal repatoms. The non-zero screw displacement of the edge dislocations suggests that each dislocation is dissociated into two  $1/6 \langle 112 \rangle$  Shockley partials bound by a stacking fault with a width of about  $19 \text{ \AA}$ . The activated slip planes are those  $\{111\}$  planes that are adjacent to the edges of the indenter. The slope for the linear part of the curve is  $27.1 \text{ GPa}$ , which is less than the shear modulus  $\mu = 33.0 \text{ GPa}$  and  $C_{44} = 29.8 \text{ GPa}$ . The critical load,  $P_{cr}$  for the homogeneous dislocation nucleation is  $18.4 \text{ N/m}$ , corresponding to a hardness of  $7.3 \text{ GPa}$  (the critical load normalized by the area of the indenter), which is  $0.22 \mu$ . The drop in applied load due to the nucleation of dislocations is  $\Delta P = 6.8 \text{ N/m}$ , agreeing with the load drop estimated by the elastic model[39] which is  $\Delta P = 7.7 \text{ N/m}$ .

For randomly distributed impurities in the Al thin film, the load-displacement curve shows a linear relation up to a depth of  $8.0 \text{ \AA}$ , followed by a drop at  $d = 8.1 \text{ \AA}$ , as shown by the

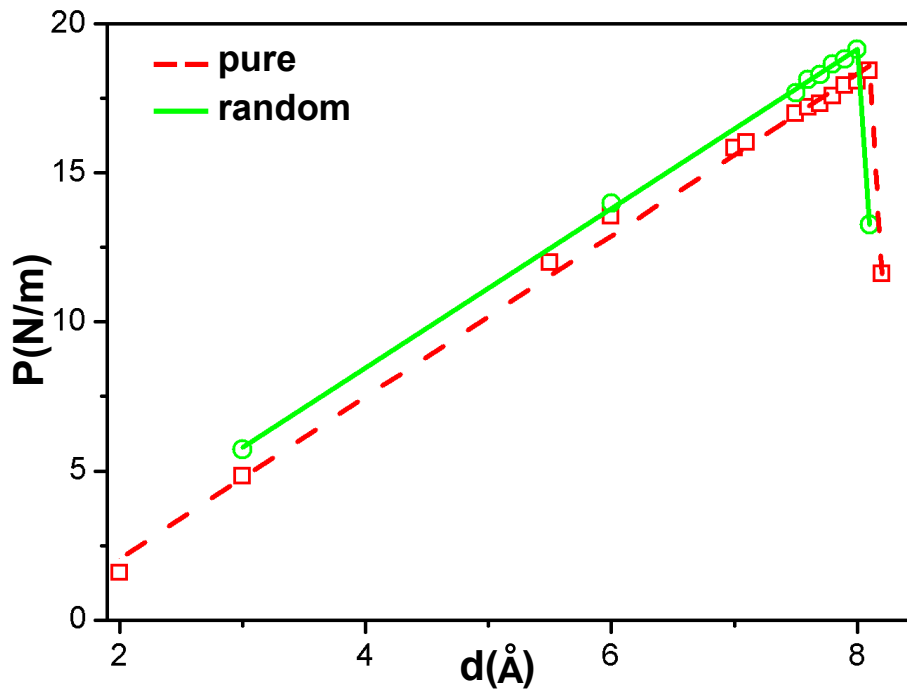


**Figure 6.** Load-displacement plot for the nanoindentation of the Al thin film with a rigid rectangular indenter: pure Al (red squares) and randomly distributed Mg impurity system (green circles). The corresponding lines are the best fit to the data points.

solid line in Fig. (8). The slope of initial linear part of the load-displacement curve is 26.7 GPa, rather close to the corresponding pure Al value. The maximum load in linear region is  $P_{cr}^{im} = 19.2$  N/m, corresponding to a hardness of 7.6 GPa, which is 0.3 GPa greater than the pure Al system. A pair of Shockley partial dislocations is nucleated at  $x=-13$  Å,  $y=-25$  Å and  $x=13$  Å,  $y=-22$  Å respectively as shown in the right panel of Fig. (9). The drop in the applied load due to the dislocation nucleation is 5.9 N/m. The estimated load drop by the elastic model is  $\Delta P = 7.6$  N/m. The smaller drop of the load for the random case than the elastic model is probably due to the presence of the Mg impurities, which is not accounted for in the elastic model [39]. The fact that the critical load and the hardness of the Al-Mg alloy are greater than that of the pure Al system demonstrates that the Mg impurities are responsible for the solid solution strengthening of the Al thin film. The presence of Mg impurities also hinders the formation of full edge dislocations and as a result, only partial dislocations are nucleated and they are pinned near the surface as shown in Fig. (9).

Finally we point out the possibility that the emitted dislocations may be somewhat constrained by the local/nonlocal interface from going further into the bulk. Because the critical stress to move an edge dislocation in Al is vanishingly small ( $10^{-5}\mu$ ) comparing to that to nucleate a dislocation ( $10^{-1}\mu$ ), a small numerical error in stress could easily lead to a large difference in the equilibrium dislocation position. The four-order-of-magnitude disparity poses a significant challenge to all atomistic simulations in predicting dislocation nucleation site, QCDF method included. One can only hope to obtain a reliable critical load for the incipient plasticity, rather than for the equilibrium position of dislocations. The same problem has been observed and discussed by others [38]. However, despite the problem, the dramatic difference observed in the two panels of Fig. 7 unambiguously demonstrates the strengthening effect of Mg impurities. Therefore the conclusion is still valid.

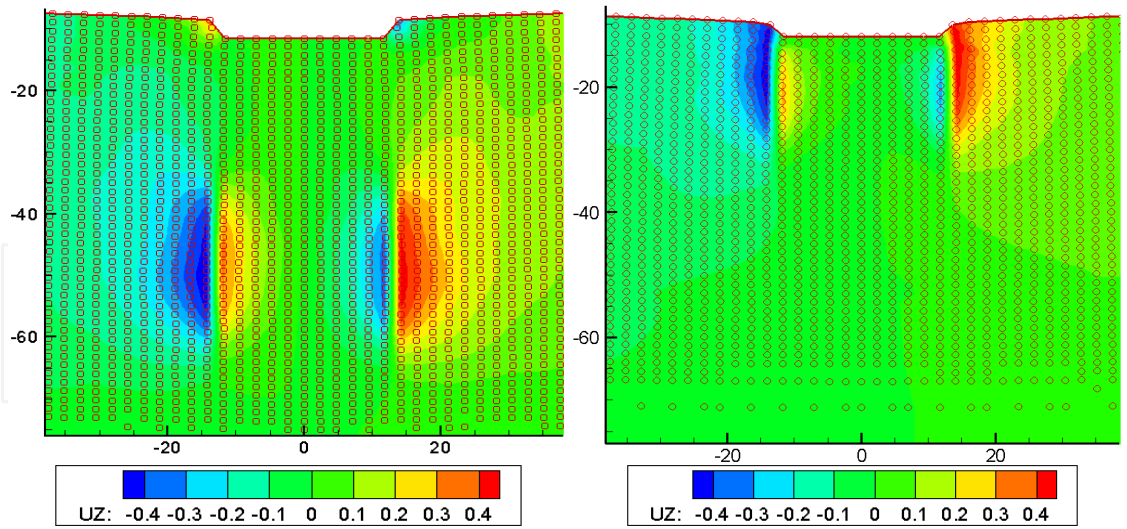


**Figure 7.** The out-of-plane displacement  $u_z$  obtained from the pure (left) and with Mg impurities (right) QCDFT calculations. The circles represent the repeatoms and the displacement ranges from  $-0.4$  (blue) to  $0.4$  (red) Å.

## 5. Solid solution effects on dislocation nucleation during nanoindentation

The load-displacement curve is the typical observable for nanoindentation, and is widely used in both experiment and theory, often serving as a link between the two. In particular, it is conventional to identify the onset of incipient plasticity with the first drop in the load-displacement curve during indentation [4, 10, 11, 13, 17, 30, 33, 35, 39, 46]. In the present work, the load is given in N/m, normalized by the length of the indenter in the out-of-plane direction.

For pure Al, the load-displacement ( $P - d$ ) curve shows a linear relation initially, followed by a drop at  $d = 8.2$  Å in Fig. (8). The drop corresponds to the homogeneous nucleation of dislocations beneath the indenter - the onset of plasticity. A pair of edge dislocations are nucleated at  $x = \pm 13$  Å, and  $y = -45$  Å. In Fig. (9), we present the out-of-plane (or screw) displacement  $u_z$  of the nonlocal repeatoms. The non-zero screw displacement of the edge dislocations suggests that each dislocation is dissociated into two  $1/6 \langle 112 \rangle$  Shockley partials bound by a stacking fault with a width of about 20 Å. The activated slip planes are  $\{111\}$  type and adjacent to the edges of the indenter. The slope for the linear part of the curve is 27.1 GPa, which is greater than the shear modulus  $\mu = 24.6$  GPa but less than  $C_{44} = 30.1$  GPa. The critical load,  $P_{cr}$  for the homogeneous dislocation nucleation is 18.4 N/m, corresponding to a hardness of 7.2 GPa. The drop in the applied load due to the nucleation of dislocations is  $\Delta P = 6.8$  N/m, similar to the value estimated by an elasticity model[39], which is  $\Delta P = 7.7$  N/m.

For randomly distributed impurities, the load-displacement curve shows a linear relation up to a depth of 8.0 Å, followed by a drop at  $d = 8.1$  Å in Fig. (8). The slope of the initial linear part of the load-displacement curve is 26.7 GPa, rather close to the corresponding pure Al value. The maximum load in linear region is  $P_{cr}^{im} = 19.2$  N/m, corresponding to a hardness of 7.5 GPa, which is 0.3 GPa or 4% greater than that of the pure Al. A pair of Shockley partial dislocations is nucleated at  $x = -13$  Å,  $y = -40$  Å and  $x = 13$  Å,  $y = -38$  Å respectively as shown in Fig. (9). The fact that the hardness of the Al-Mg alloy is greater than that of the pure Al is an indication of solid solution strengthening. However, the magnitude of the strengthening

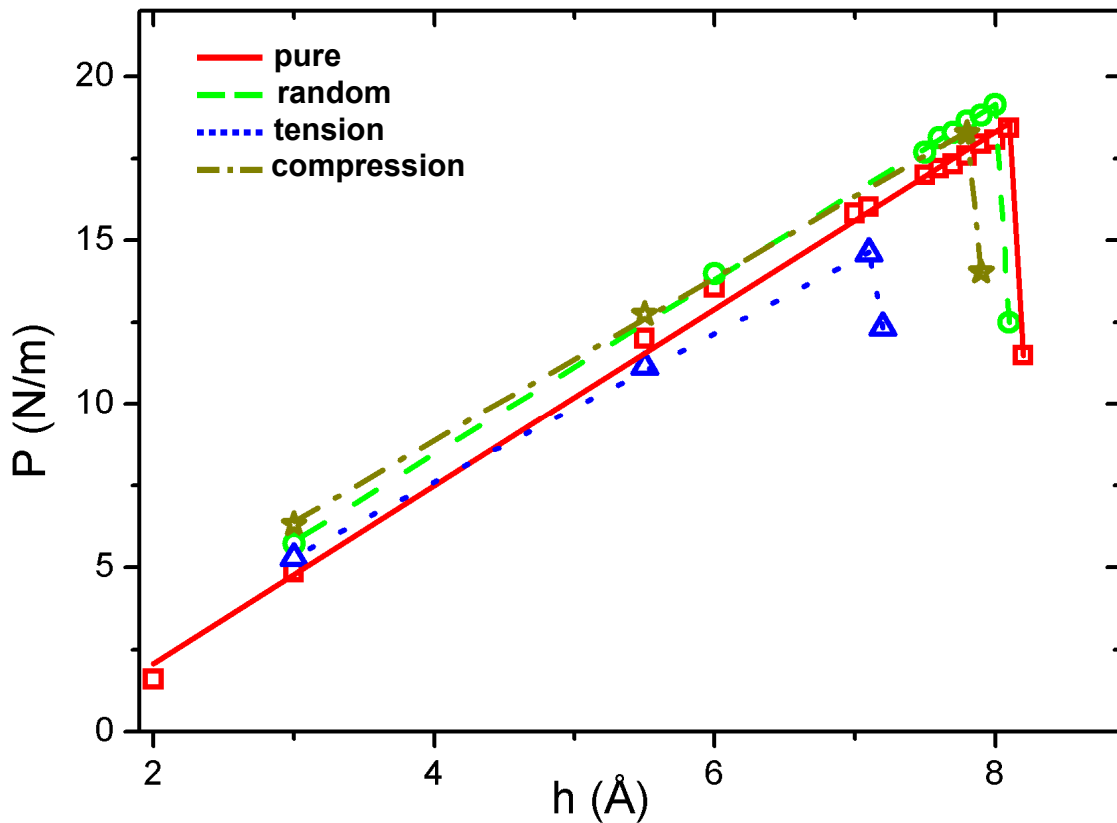


**Figure 8.** Load-displacement plot for the nanoindentation of the Al thin film with a rigid rectangular indenter: *pure* (solid line), *random* (dashed line), *tension* (dotted line), *compression* (dash-dotted line) obtained from QCDFE calculations. The lines are the best fit to the corresponding simulation data points.

is insignificant, and is on the order of the changes in the shear modulus. This finding is consistent to an experimental study on Cu-Ni solid solution alloys [1] the nanoindentation measurements demonstrated the effects of solute impurities on the formation of dislocations in a previously dislocation-free region to be minimal. Moreover, the experimental study suggested that overall dislocation nucleation is strongly related to shear modulus in this system. It is clear from our results that the origin of the strengthening is not due to the propagation of dislocations, but rather the nucleation of the dislocations. The presence of randomly distributed Mg impurities hinders the nucleation of dislocations. In fact, only the leading partial dislocations are nucleated trailing by stacking faults as shown in Fig. (9)b. This result is in contrast to the pure system where full dislocations are nucleated at a larger distance below the surface. The drop in the applied load due to incipient plasticity is 5.9 N/m, less than that of the pure system (6.8 N/m). The smaller drop of the load in the random case is due to the fact that the partial dislocations are nucleated instead of full dislocations as in the pure system. We expect that the critical load/hardness corresponding to the nucleation of full dislocations in this case will be higher because of work hardening.

The reason why partial dislocations are nucleated as opposed to full dislocations in the presence of random impurities can be understood from the following energetic consideration. The total energy of the system can be approximated by the dislocation elastic energy and the stacking fault energy. The former is given by  $\frac{\mu}{2\pi(1-\nu)}b^2$  where  $\mu$ ,  $\nu$  and  $b$  are the shear modulus, Poisson's ratio and Burgers vector, respectively. The latter energy can be expressed as  $\gamma \times w$  where  $\gamma$  is the ISF energy and  $w$  is the width of the stacking fault. Because  $\mu$  is

	<i>pure</i>	<i>random</i>	<i>compression</i>	<i>tension</i>
$\mu$ [GPa]	24.55	25.08	25.07	25.07
$\gamma_{\text{isf}}$ [J/m <sup>2</sup> ]	0.12	0.11	0.11	0.11
$b$	2.85	1.65	1.65	1.65
$w$ [Å]	20,20	32,30	28	7
$E_{\text{tot}}$ [eV]	3.94	3.03	1.37	0.67

**Table 2.** The shear modulus  $\mu$ , intrinsic stacking fault energy  $\gamma_{\text{isf}}$ , Burgers vector, stacking fault width and the approximate total energy for the dislocations, corresponding to the *pure*, *random*, *compression*, and *tension* cases.

increased in the presence of the impurities, the system could lower its energy by reducing  $b$ , i.e., dissociation into partials. Of course, it is energetic favorable only if the  $\gamma$  and  $w$  are not too large. The fact the  $\gamma$  value is slightly reduced in the presence of Mg impurities helps the dissociation. Using the quantities tabulated in Table II, we find that the total energy of the random impurities system (with two partial dislocations) is 0.91 eV lower than that of the pure system (two full dislocations). In Table II, the Burgers vectors for full and partial dislocation are determined to be 2.85 Å and 1.65 Å respectively. The width of the stacking fault ( $w$ ) has two entries for the pure and random cases since there are two dislocations nucleated.

For Mg impurities below the slip plane as in the *tension* case, the load-displacement curve shows a linear relation up to a depth of 7.1 Å, followed by a drop at  $d = 7.2$  Å (dotted line in Fig. (8)). The maximum load in linear region is  $P_{cr}^{im} = 17.8$  N/m, corresponding to a hardness of 6.5 GPa, which is 0.7 GPa or 10 % smaller than the pure Al system. A single Shockley partial dislocation is nucleated at  $x=-13$  Å,  $y=-14$  Å as shown in Fig. (9). The drop in the applied load due to the dislocation nucleation is 2.3 N/m.

Similarly, for Mg impurities above the slip plane as in the *compression* case, the load-displacement curve is linear up to a depth of 7.8 Å, followed by a drop at  $d = 7.9$  Å, as shown by the dot-dashed line in Fig. (8). The maximum load in linear region is  $P_{cr}^{im} = 18.3$  N/m, corresponding to a hardness of 7.1 GPa, which is 0.1 GPa smaller than the pure Al system. A single Shockley partial dislocation is nucleated at  $x=-13$  Å,  $y=-35$  Å in Fig. (9). The drop in the applied load due to the dislocation nucleation is 4.2 N/m.

From the above results, we conclude that the linear distribution of Mg impurities can actually soften the material and render dislocation nucleation easier than the pure system. In other words, the solid solution strengthening effect depends sensitively on the local configuration of the impurities. In the three cases (of the same Mg concentration) studied here, the hardness of the alloys varies and the impurities can either increase or decrease the hardness, depending on their configuration. It should be emphasized that the change in hardness is associated with dislocation nucleation, not with dislocation propagation. Although it is well-known that dislocation propagation (or dislocation-impurity interaction) depends sensitively on the impurity configuration, it is less recognized that the impurities configuration is important for dislocation nucleation.

The reason that the hardness in the tension case is less than that in the compression case can be understood from the atomic size consideration. The atomic or ionic radius of Al is 0.54 Å, which is less than that of Mg (0.86 Å). In the compression case, since smaller Al atoms are replaced by larger Mg atoms in a compression region, the substitution increases the compressive stress, and makes it more difficult to form edge dislocations, thus a higher

hardness. On the other hand, the replacement of smaller Al atoms by larger Mg atoms in a tension region reduces the tension and makes it easier to form the dislocations, hence a lower hardness. Because the impurities are located on one side of the indenter - the symmetry is broken, dislocation is also nucleated at one side of the thin film. Because only one partial dislocation is nucleated in the compression and tension cases, the energy of the two cases is much smaller as shown Table II.

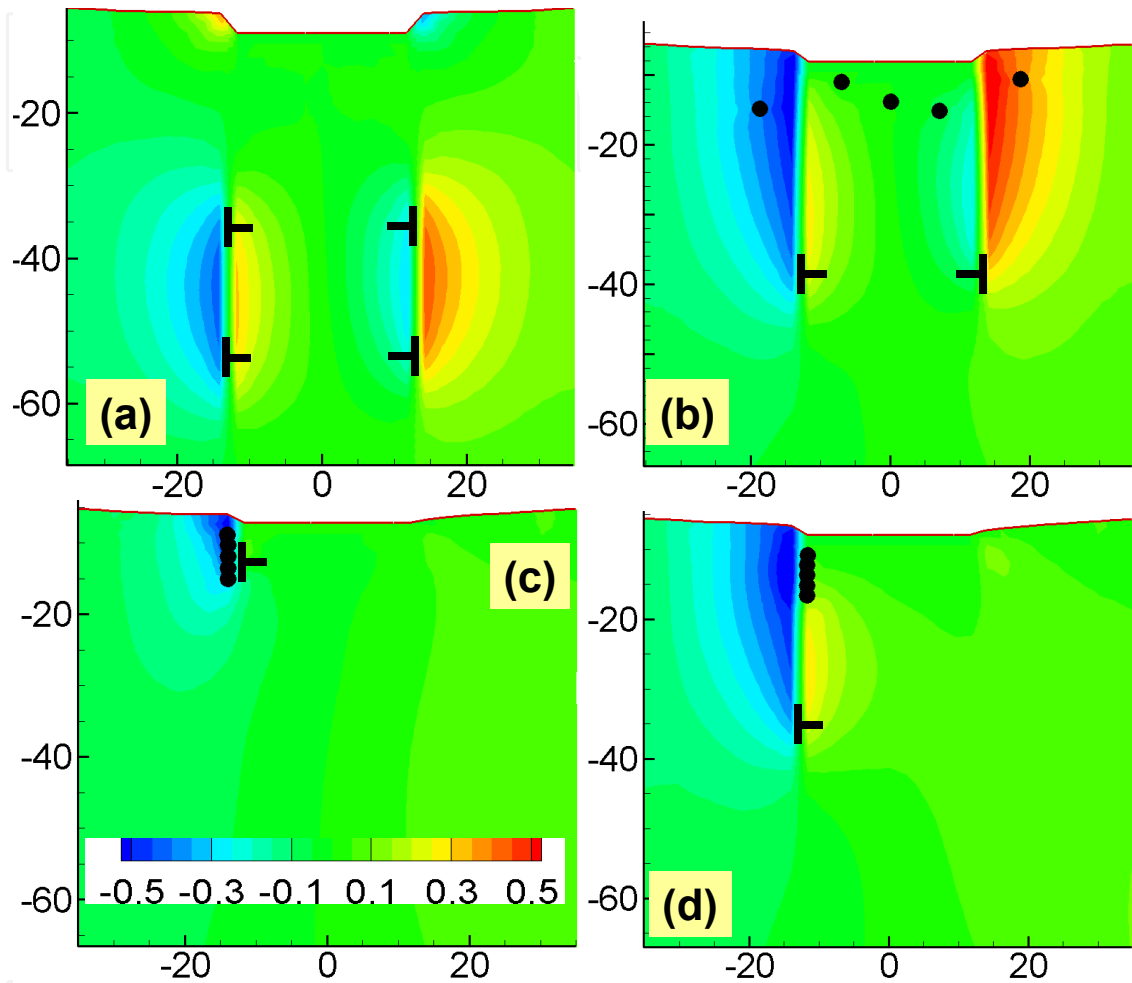


**Figure 9.** The out-of-plane displacement  $u_z$  corresponding to (a) *pure*, (b) *random*, (c) *tension*, (d) *compression* cases obtained from QCDFE calculations. The displacement ranges from -0.5 (blue) to 0.5 (red) Å. The black dots indicate the position of the Mg impurities. All distances are given in Å.

## 6. Conclusions

We presented a concurrent multiscale method that makes it possible to simulate multi-million atoms based on density functional theory. The method - QCDFE - is formulated within the framework of the QC method, with OFDFT as its sole input, i.e., there is only one underlying energy functional (OFDFT) involved. Full-blown OFDFT and OFDFT-based elasticity theory are the two limiting cases corresponding to a fully nonlocal or a fully local version of QCDFE. The QC ghost force at the local-nonlocal interface is corrected by a dead load approximation. The QCDFE method is applied for a nanoindentation study of an Al thin film. The QCDFE results are validated by comparing against conventional QC with a OFDFT-refined EAM

potential. The results suggest that QCDFT is an excellent method for quantum simulation of materials properties at length scales relevant to experiments.

For the study of the nanoindentation of an Al thin film in the presence and absence of randomly distributed Mg impurities, the Mg impurities are found to strengthen the hardness of Al and hinder the dislocation nucleation. The results suggest that QCDFT is a promising method for quantum simulation of materials properties at length scales relevant to experiments.

We also find that the solid solution effect depends sensitively on the local configuration of the impurities. Although a random distribution of the impurities increases the hardness of the material, linear distributions of the impurities actually lower the hardness. In both cases, the effects are entirely due to dislocation nucleation; the solid solution strengthening owing to dislocation motion is not considered here. Consistent to the experimental results on Ni/Cu alloys, the extent of the solid solution strengthening is found to be insignificant - in the same order of magnitude of the change in shear modulus. On the other hand, the incipient plasticity is observed to be quite different among the different cases. In the pure material, two full dislocations are nucleated under the indenter with the opposite sign. For the random distribution of the impurities, two partial dislocations are nucleated instead. For the linear distributions of the impurities, only one partial dislocation is nucleated.

The QCDFT method could be used for other FCC materials, such as gold and copper. Besides materials with FCC lattice, QCDFT method could be directly used to study the BCC (body-centered-cubic) materials, iron and its alloys for example. It will be also applicable for complex lattice structures, such as hexagonal close-packed (hcp) structures, magnesium and its alloys for example.

## Author details

Qing Peng

Department of Mechanical, Aerospace and Nuclear Engineering, Rensselaer Polytechnic Institute, Troy, NY 12180, USA

## 7. References

- [1] Bahr, D. & Vasquez, G. [2005]. Effect of solid solution impurities on dislocation nucleation during nanoindentation, *J. Mater. Res.* 20(8): 1947–1951.
- [2] Chen, M., Ma, E., Hemker, K. J., Sheng, H., Wang, Y. & Cheng, X. [2003]. Deformation twinning in nanocrystalline aluminum, *Science* 300(5623): 1275.
- [3] Choly, N., Lu, G., E, W. & Kaxiras, E. [2005]. Multiscale simulations in simple metals: A density-functional-based methodology, *Phys. Rev. B* 71(9): 094101.
- [4] Corcoran, S. G., Colton, R. J., Lilleodden, E. T. & Gerberich, W. W. [1997]. Anomalous plastic deformation at surfaces: Nanoindentation of gold single crystals, *Phys. Rev. B* 55(24): R16057–R16060.
- [5] Ercolessi, F. & Adams, J. B. [1994]. Interatomic potentials from 1st-principles calculations - the force-matching method, *Europhys. Lett.* 26(8): 583–588.
- [6] Fischer-Cripps, A. C. [2004]. *Nanoindentation*, Vol. 2nd ed., Springer-Verlag, New York. pp 1.
- [7] Gao, J. & Truhlar, D. G. [2002]. Quantum mechanical methods for enzyme kinetics, *Annu. Rev. Phys. Chem.* 53: 467.

- [8] Gerberich, W., Nelson, J., Lilleodden, E., Anderson, P. & Wyrobek, J. [1996]. Indentation induced dislocation nucleation: The initial yield point, *Acta Materialia* 44: 3585–3598.
- [9] Goodwin, L., Needs, R. J. & Heine, V. [1990]. A pseudopotential total energy study of impurity-promoted intergranular embrittlement, *J. Phys. Condens. Matter* 2: 351.
- [10] Gouldstone, A., Chollacoop, N., Dao, M., Li, J., Minor, A. M. & Shen, Y.-L. [2007]. Indentation across size scales and disciplines: Recent developments in experimentation and modeling, *Acta Mater.* 55(12): 4015 – 4039.
- [11] Gouldstone, A., Koh, H. J., Zeng, K. Y., Giannakopoulos, A. E. & Suresh, S. [2000]. Discrete and continuous deformation during nanoindentation of thin films, *Acta Mater.* 48(9): 2277 – 2295.
- [12] Gouldstone, A., Van Vliet, K. J. & Suresh, S. [2001]. Nanoindentation - Simulation of defect nucleation in a crystal, *NATURE* 411(6838): 656.
- [13] Hayes, R. L., Fago, M., Ortiz, M. & Carter, E. A. [2005]. Prediction of dislocation nucleation during nanoindentation by the orbital-free density functional theory local quasi-continuum method, *Multiscale Mod. Sim.* 4: 359.
- [14] Hayes, R. L., Ho, G., Ortiz, M. & Carter, E. A. [2006]. Prediction of dislocation nucleation during nanoindentation of Al3Mg by the orbital-free density functional theory local quasiconinuum method, *Philos. Mag.* 86: 2343.
- [15] Hung, L. & Carter, E. A. [2009]. Accurate simulations of metals at the mesoscale: Explicit treatment of 1 million atoms with quantum mechanics, *Chemical Physics Letters* 475(4-6): 163 – 170.
- [16] Kelchner, C. L., Plimpton, S. J. & Hamilton, J. C. [1998]. Dislocation nucleation and defect structure during surface indentation, *PHYSICAL REVIEW B* 58(17): 11085–11088.
- [17] Knap, J. & Ortiz, M. [2003]. Effect of indenter-radius size on au(001) nanoindentation, *Phys. Rev. Lett.* 90(22): 226102.
- [18] Kohn, W. [1995]. Density functional theory for systems of very many atoms, *Int. J. Quantum Chem.* 56: 229.
- [19] Kohn, W. & Sham, L. J. [1965]. Self-consistent equations including exchange and correlation effects, *Phys. Rev.* 140(4A): A1133–A1138.
- [20] Liao, X. Z., Zhou, F., Lavernia, E. J., He, D. W. & Zhu, Y. T. [2003]. Deformation twins in nanocrystalline Al, *Appl. Phys. Lett.* 83(24): 5062.
- [21] Lignères, V. & Carter, E. [2005]. *Handbook of Materials Modeling*, Springer, Dordrecht, The Netherlands, pp. 127–148.
- [22] Lin, H. & Truhlar, D. G. [2007]. QM/MM: What have we learned, where are we, and where do we go from here?, *Theor. Chem. Acc.* 117: 185.
- [23] Lu, G., Peng, Q., Zhang, X., Hung, L. & Carter, E. A. [2008]. Quantum simulation of materials at micron scales and beyond, *Oberwolfach Reports* 5(2): 1117.
- [24] Mordasini, T. & Thiel, W. [1998]. Combined quantum mechanical and molecular mechanical approaches, *Chimia* 52: 288.
- [25] NIX, W. D. [1989]. Mechanical-properties of thin-films, *METALLURGICAL TRANSACTIONS A-PHYSICAL METALLURGY AND MATERIALS SCIENCE* 20(11): 2217.
- [26] Oliver, W. & Pharr, G. [1992]. An improved technique for determining hardness and elastic modulus using load and displacement sensing indentation experiments, *J. Mater. Res.* 7(6): 1564–1583.
- [27] Page, T. F., Oliver, W. C. & McHargue, C. J. [1992]. The deformation-behavior of ceramic crystals subjected to very low load (nano)indentations, *J. Mater. Res.* 7(2): 450–473.

- [28] Peng, Q. & Lu, G. [2011]. A comparative study of fracture in Al: Quantum mechanical vs. empirical atomistic description, *JOURNAL OF THE MECHANICS AND PHYSICS OF SOLIDS* 59(4): 775–786.
- [29] Peng, Q., Zhang, X., Huang, C., Carter, E. A. & Lu, G. [2010]. Quantum mechanical study of solid solution effects on dislocation nucleation during nanoindentation, *MODELLING AND SIMULATION IN MATERIALS SCIENCE AND ENGINEERING* 18(7): 075003.
- [30] Peng, Q., Zhang, X., Hung, L., Carter, E. A. & Lu, G. [2008]. Quantum simulation of materials at micron scales and beyond, *Phys. Rev. B* 78: 054118.
- [31] Peng, Q., Zhang, X. & Lu, G. [2010]. Quantum mechanical simulations of nanoindentation of Al thin film, *COMPUTATIONAL MATERIALS SCIENCE* 47(3): 769.
- [32] Shenoy, V. B., Miller, R., Tadmor, E. B., Rodney, D., Phillips, R. & Ortiz, M. [1999]. An adaptive finite element approach to atomic-scale mechanics - the quasicontinuum method, *J. Mech. Phys. Solids* 47: 611.
- [33] Shenoy, V. B., Phillips, R. & Tadmor, E. B. [2000]. Nucleation of dislocations beneath a plane strain indenter, *J. Mech. Phys. Solids* 48(4): 649 – 673.
- [34] Sherwood, P. [2000]. *Modern Methods and Algorithms of Quantum Chemistry*, Vol. 3, NIC, Princeton, p. 285.
- [35] Suresh, S., Nieh, T. G. & Choi, B. W. [1999]. Nano-indentation of copper thin films on silicon substrates, *Scripta Materialia* 41(9): 951 – 957.
- [36] T. K. Woo, P. M. Margl, L. D. L. C. & Ziegler, T. [n.d.]. *ACS Symp. Ser.* .
- [37] Tadmor, E. B. & Miller, R. E. [2005]. *Handbook of Materials Modeling*, Vol. 1, Kluwer Academic Publishers, chapter The Theory and Implementation of the Quasicontinuum Method.
- [38] Tadmor, E. B., Miller, R. & Phillips, R. [1999]. Nanoindentation and incipient plasticity, *J. Mater. Res.* 14: 2249.
- [39] Tadmor, E. B., Miller, R., R., P. & Ortiz, M. [1999]. Nanoindentation and incipient plasticity, *J. Mater. Res.* 14: 2233.
- [40] Tadmor, E. B., Ortiz, M. & Phillips, R. [1996]. Quasicontinuum analysis of defects in solids, *Philos. Mag. A* 73: 1529.
- [41] Wang, Y. A. & Carter, E. A. [2000]. *Theoretical Methods in Condensed Phase Chemistry*, Dordrecht, Kluwer, chapter 5.
- [42] Wang, Y. A., Govind, N. & Carter, E. A. [1999]. Orbital-free kinetic-energy density functionals with a density-dependent kernel, *Phys. Rev. B* 60: 16350.
- [43] Zhang, X. & Lu, G. [2007]. Quantum mechanics/molecular mechanics methodology for metals based on orbital-free density functional theory, *Phys. Rev. B* 76: 245111.
- [44] Zhang, X., Peng, Q. & Lu, G. [2010]. Self-consistent embedding quantum mechanics/molecular mechanics method with applications to metals, *Phys. Rev. B* 82: 134120.
- [45] Zhao, Y., Wang, C., Peng, Q. & Lu, G. [2010]. Error analysis and applications of a general QM/MM approach, *COMPUTATIONAL MATERIALS SCIENCE* 50(2): 714–719.
- [46] Zhu, T., Li, J., Vliet, K. J. V., Ogata, S., Yip, S. & Suresh, S. [2004]. Predictive modeling of nanoindentation-induced homogeneous dislocation nucleation in copper, *J. Mech. Phys. Solids* 52(3): 691 – 724.
- [47] Zienkiewicz, O. C. & Taylor, R. L. [2000]. *the Finite Element Method*, Vol. 1, Oxford, Butterworth-Heinemann. pp 23.
- [48] Zimmerman, J. A., Kelchner, C. L., Klein, P. A., Hamilton, J. C. & Foiles, S. M. [2001]. Surface step effects on nanoindentation, *PHYSICAL REVIEW LETTERS* 87(16): art. no.–165507.